JACS
JOURNAL OF THE AMERICAN CHEMICAL SOCIETY
Article
pubs.acs.org/JACS

An Optically Transparent Iron Nickel Oxide Catalyst for Solar Water Splitting

Carlos G. Morales-Guio,[†] Matthew T. Mayer,[‡] Aswani Yella,[‡,§] S. David Tilley,[‡,#] Michael Grätzel,[‡] and Xile Hu*[,†]

[†]Laboratory of Inorganic Synthesis and Catalysis, Institute of Chemical Sciences and Engineering, École Polytechnique Fédérale de Lausanne (EPFL), 1015 Lausanne, Switzerland

[‡]Laboratory of Photonics and Interfaces, Institute of Chemical Sciences and Engineering, École Polytechnique Fédérale de Lausanne (EPFL), 1015 Lausanne, Switzerland

Supporting Information

ABSTRACT: Sunlight-driven water splitting to produce hydrogen fuel is an attractive method for renewable energy conversion. Tandem photoelectrochemical water splitting devices utilize two photoabsorbers to harvest the sunlight and drive the water splitting reaction. The absorption of sunlight by electrocatalysts is a severe problem for tandem water splitting devices where light needs to be transmitted through the larger bandgap component to illuminate the smaller bandgap component. Herein, we describe a novel method for the deposition of an optically transparent amorphous iron nickel oxide oxygen evolution electrocatalyst. The catalyst was deposited on both thin film and high-aspect ratio nanostructured hematite photoanodes. The low catalyst loading combined with its high activity at low overpotential results in significant improvement on the onset potential for photoelectrochemical water oxidation. This transparent catalyst further enables the preparation of a stable hematite/perovskite solar cell tandem device, which performs unassisted water splitting.

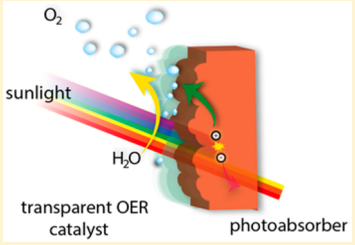

INTRODUCTION

The conversion of solar energy into chemical fuels is a promising method for solar energy storage.[1,2] Photoelectrochemical (PEC) cells mimic photosynthesis in plants by integrating in the same device energy capture from sunlight and the generation of molecular fuels, such as hydrogen. However, artificial photosynthetic systems may be engineered into configurations more efficient than those found in nature. An integrated tandem PEC water splitting device (Figure 1) uses two photoabsorbers to harvest sunlight and drive the reaction. In such a tandem device, light transmitted through the top semiconductor is absorbed in a smaller band gap photoelectrode underneath to provide the necessary photovoltage for unassisted water splitting, analogous to the Z-scheme found in the plant's chloroplast.[2] These dual-absorber tandem PEC systems have been predicted to reach over 25% solar-to-hydrogen conversion (STH) efficiency when realistic energy losses are taken into account.[3,4] To date, various artificial photosynthetic systems have been proposed,[5−7] and monolithic devices with STH efficiency of up to 18% have been experimentally demonstrated.[8] However, these high efficiency devices employ expensive photoabsorbers and noble metal electrocatalysts, which are prohibitive for large scale application.

Many Earth-abundant oxygen evolution reaction (OER) electrocatalysts have been recently reported[9−15] and some of them have been coupled to inexpensive photoanodes such as Hematite (α-Fe_2O_3), $BiVO_4$, and WO_3 for PEC water oxidation.[16−23] Among these catalysts, nickel−iron oxides ($NiFeO_x$) are some of the most active OER catalysts in alkaline solution.[10,11,13,14,24] Recently, Wang and co-workers used photodecomposition of a Ni- and Fe-containing metal−organic precursor[10] to deposit $NiFeO_x$ on hematite.[20] The catalyst significantly shifted the onset potential of the OER;

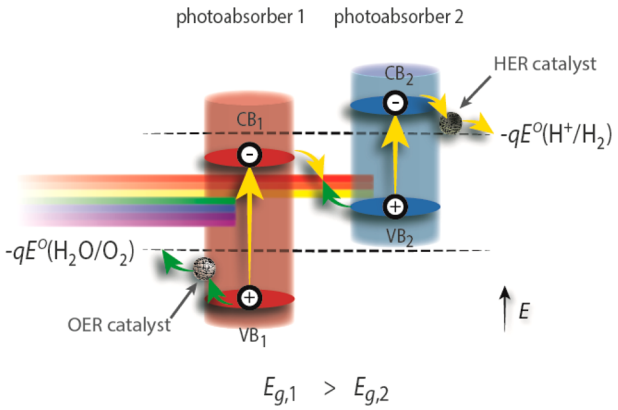

Figure 1. Photoelectrochemical tandem cell schematic. Z-scheme of artificial photosynthesis driven by the absorption of two photons, one at photoabsorber 1 to evolve oxygen and the other at photoabsorber 2 to evolve hydrogen. Oxygen- and hydrogen-evolution catalysts are shown to illustrate the facilitation of hole and electron transfer across the electrolyte/semiconductor interface. Dotted lines indicate the thermodynamic reduction and oxidation potentials of water.

Received: May 29, 2015
Published: July 22, 2015

DOI: 10.1021/jacs.5b05544
J. Am. Chem. Soc. 2015, 137, 9927−9936

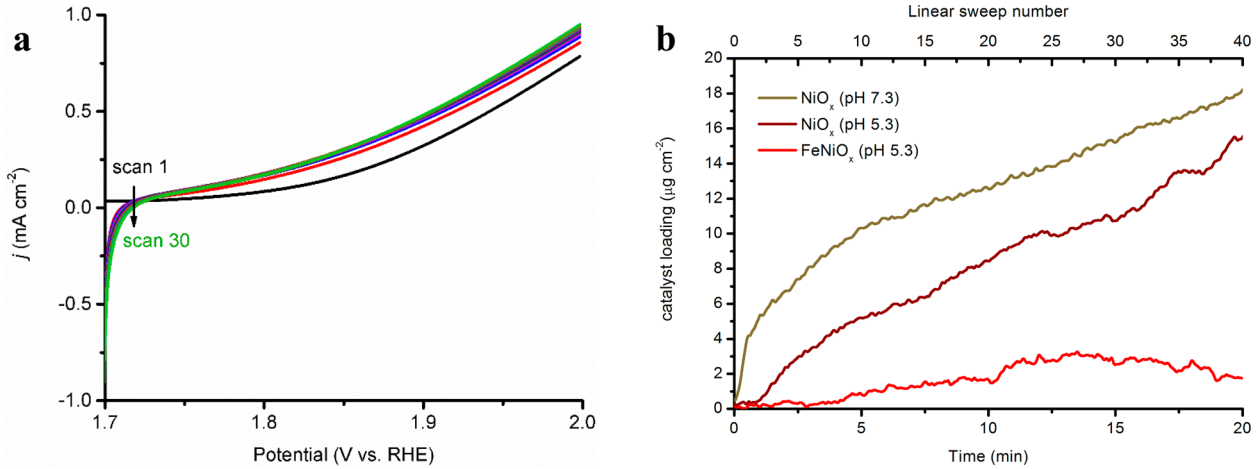

Figure 2. Electrochemical deposition of metal oxide-hydroxide materials. (a) Typical potential−current density curves during electrodeposition of a NiO_x (pH 7.3) catalyst by linear sweep voltammetry from 1.7 to 2.0 V vs RHE at 10 mV s^{-1}. Conditions: Au substrate, 16 mM nickel(II) acetate, 0.1 M sodium acetate, 10 mV s^{-1}, pH = 7.3. (b) Time-dependent evolution of catalyst mass loading at different conditions, monitored by in situ quartz crystal microbalance. Conditions: Au substrate, linear sweeps from 1.7 to 2.0 V vs RHE at 10 mV s^{-1}. The concentration of nickel(II) acetate in the three solutions is 16 mM with a supporting electrolyte concentration (sodium acetate) of 0.1 M. The solution containing the iron(III) precursor has an $Fe_2(SO_4)_3$ concentration of 5 mM. The natural pH of the solution for nickel(II) acetate is 7.3 and the natural pH of the solution containing the Fe and Ni precursors is 5.3. The Ni(II) pH 5.3 solution was obtained through controlled addition of acetic acid.

however, backside illumination was necessary due to strong light absorption by the thick catalyst layer. In fact, due to the parasitic light absorption by the OER catalysts on the front side, photoanodes coated with OER catalysts often must be illuminated from the back (photoabsorber side).[25] However, in conventional tandem device configurations,[26] the illumination of a photoanode has to be done from the front (catalyst) side to allow light absorption by the smaller bandgap photoabsorber beneath (Figure 1). The implementation of dichroic mirrors has been considered as an alternative option to circumvent parasitic light absorption in a PEC cell. However, such a configuration has not been realized. Therefore, the necessity of optically transparent OER catalysts for solar water splitting, especially when nanostructured, high-surface-area photoanodes are used as the photoabsorbers, has been recently recognized.[25,27,28] While a number of optical transparent catalysts are reported,[29] the coupling of these catalysts to photoanodes is rarely reported. Herein, we report a novel method for the conformal deposition of a highly efficient iron nickel oxide ($FeNiO_x$) OER catalyst. The catalyst has a very high turnover frequency for the OER, comparable to that of noble metal catalysts. The low catalyst loading required to achieve high current densities at low overpotential results in very low optical losses, rendering the catalyst virtually transparent. As a demonstration of principle, we show that this transparent catalyst promotes OER on both flat and nanostructured hematite photoanodes in a front illumination configuration. Moreover, the catalyst allows the configuration of a tandem hematite/perovskite solar cell tandem device, which performs unassisted water splitting with STH efficiency over 1.9%.

RESULTS AND DISCUSION

Electrochemical Deposition of OER Catalysts. The electrodeposition methods for active $NiFeO_x$ catalysts reported to-date[13,24,30−35] require slightly acidic solutions (pH < 6) and the application of potentials more negative than the thermodynamic hydrogen evolution potential. Hematite dissolves at acidic pH values in the range of potentials required for cathodic deposition of $NiFeO_x$ catalysts (generally, −0.5 to −1.0 V vs the standard hydrogen electrode). Thus, the development of electrodeposition methods for $NiFeO_x$ oxides at positive potentials where hematite is the stable form of iron in solution is of high interest.

Amorphous porous nickel oxide-hydroxide, on the other hand, can be deposited on conductive electrodes through direct oxidative deposition of a Ni^{2+} precursor in aqueous solution at neutral pH and room temperature.[36−38] Figure 2a shows typical current−potential curves observed during the deposition of Ni oxide-hydroxide by linear sweep voltammetry between 1.7 and 2.0 V vs RHE in an aqueous solution of nickel(II) acetate at pH = 7.3. This material is labeled as NiO_x (pH 7.3) to indicate the nature of the metal oxide-hydroxide and the pH of the solution used during its electrodeposition. The change in catalyst loading with time during the electrochemical deposition was determined by electrochemical quartz crystal microbalance (EQCM). Figure 2b shows the evolution of mass during the deposition of NiO_x at pH 7.3. The initial linear sweeps lead to fast nucleation and growth of the NiO_x material. After a few linear sweeps the film growth approaches a constant rate.

The addition of iron to nickel oxide catalysts is known to improve the OER activity. However, to the best of our knowledge, an electrochemical method for the deposition of $NiFeO_x$ catalyst under anodic current flow, where many metal oxide photoanodes (including hematite) are stable, has not been reported. The photodeposition method of Berlinguette[10] was attempted for the nanostructured hematite photoanodes, nano-Fe_2O_3, developed in our laboratories.[39] With front side illumination, light absorption by the catalyst largely diminished the photocurrents, as shown in Figure S1. Dilution of the catalyst precursor solution reduces parasitic light absorbance by the catalyst. However, no real improvement in the onset potential was observed, whether by front or rear illumination, for the case of our nanostructured electrodes. Therefore, we decided to develop a new anodic electrochemical deposition method for nickel−iron oxide catalysts.

Addition of 0.31 equiv of $Fe_2(SO_4)_3$ (Fe(III) sulfate) to a solution of 16 mM Ni(II) acetate lowered the pH from 7.3 to

DOI: 10.1021/jacs.5b05544
J. Am. Chem. Soc. 2015, 137, 9927−9936

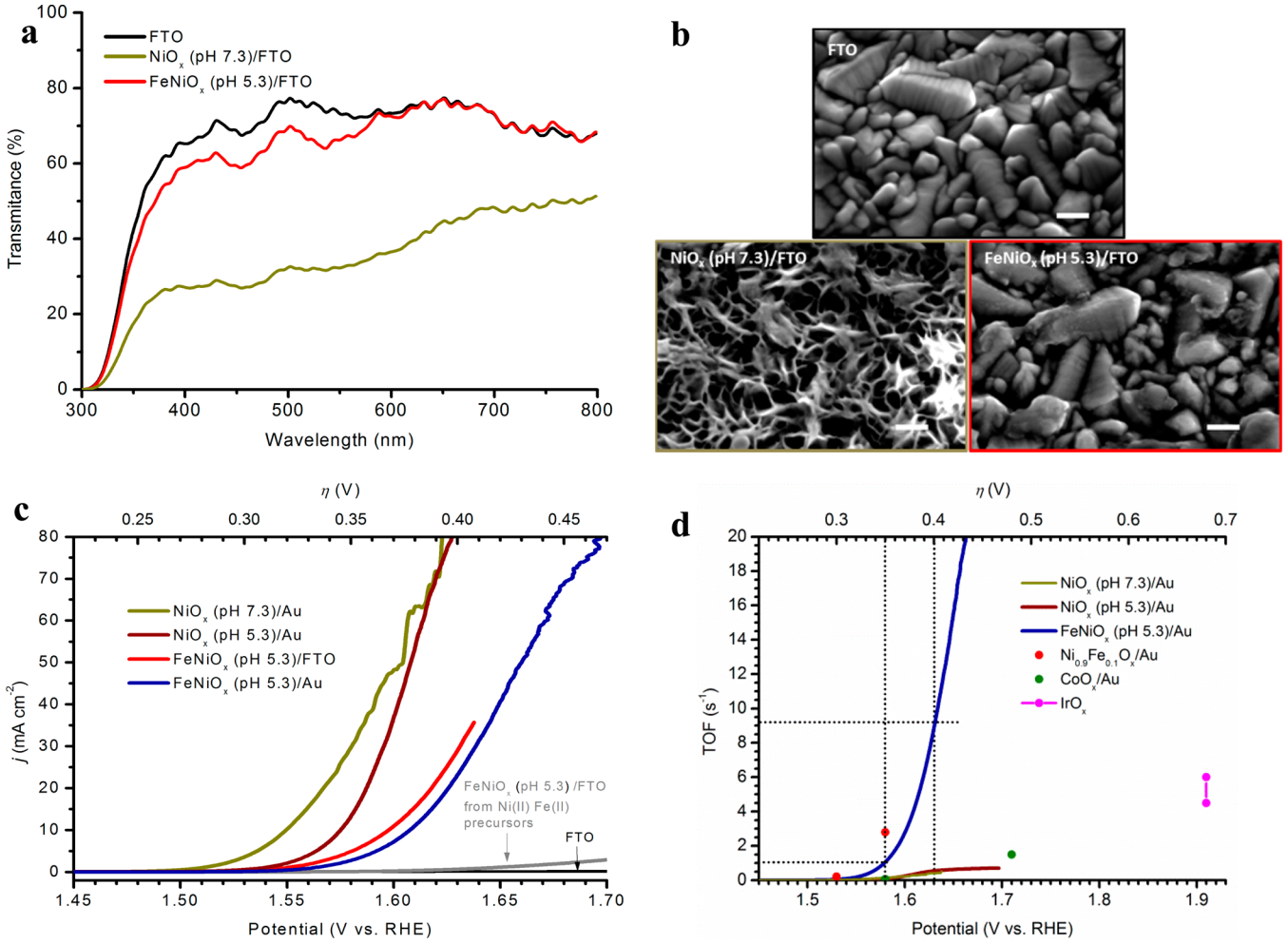

Figure 3. Characterization and OER activity of NiO_x and $FeNiO_x$. (a) Transmittance spectra of NiO_x and $FeNiO_x$ on FTO. The catalysts were deposited by 150 linear sweeps. (b) SEM images of NiO_x and $FeNiO_x$ electrodeposited on FTO. Scale bar corresponds to 100 nm. (c) Polarization curves of NiO_x and $FeNiO_x$ catalysts corrected for *iR* drop (~4 Ω cm^2). All electrochemical measurements were done in a 1 M KOH solution at pH 13.6. The scan rate is 5 mV s^{-1}; the scan direction is toward more positive potential on the RHE scale. (d) TOFs of NiO_x and $FeNiO_x$ electrocatalysts compared to other OER catalysts. The TOFs of NiO_x and $FeNiO_x$ were determined assuming all Ni ions in these catalysts are active. These TOFs represent the lower limit of the real TOFs. TOFs for $Ni_{0.9}Fe_{0.1}O_x$/Au and CoO_x/Au in 1 M KOH were taken from ref 14. TOF values for IrO_x nanoparticles at pH 7 are taken from ref 42. The overpotential for water oxidation by IrO_x nanoparticles is independent of pH between pH 1.5 and 13.

5.3. This solution was stable in air for at least 24 h. A mixed Ni and Fe oxide film could be deposited by linear sweep voltammetry between 1.7 and 2.0 V vs RHE (Figure S2). The electrodeposition worked similarly in air or under nitrogen. X-ray photoelectron spectroscopy (XPS) analysis of the film shows a Fe:Ni ratio of 80:20 (Figure S3). This film has a much higher Fe content than conventional $NiFeO_x$ films where the Fe composition ranges between 10% and 50%.[11,13,30] Therefore, the new film is labeled as $FeNiO_x$ in contrast to the nickel-rich $NiFeO_x$ catalysts. Detailed description of the XPS data fitting and assignment of metal oxidation state to the different peaks is given in the Supporting Information. Surprisingly, the growth of the $FeNiO_x$ film was slowed by at least 1 order of magnitude (Figure 2b) compared to the growth of the NiO_x film under the same conditions.[40] To probe whether this was an effect of pH, NiO_x film was also deposited at pH 5.3. Figure 2b shows that the growth of NiO_x at this pH was indeed slower than at pH 7.3, confirming an effect of pH. However, the growth rate of NiO_x at pH 5.3 was still much faster than that of the $FeNiO_x$ film. A plausible explanation is that the corrosion of the NiO_x film is faster at lower pHs, and Fe ions further accelerate the corrosion because they are Lewis acidic. It was noted that deposition of the $FeNiO_x$ catalyst using Fe(II) sulfate under otherwise identical conditions was unsuccessful.

As the amount of $FeNiO_x$ deposited using the new method was very small, the $FeNiO_x$ film appeared colorless on FTO. UV−vis transmittance spectra of the NiO_x and $FeNiO_x$ catalysts are shown in Figure 3a. Deposition of $FeNiO_x$ catalyst on FTO had only a slight effect on the transmittance of light while deposition of NiO_x catalyst greatly reduced the transmittance in the visible region. Normalization of light absorbance by unit of mass shows similar light absorbance by the NiO_x and $FeNiO_x$ catalysts after activation for electrochemical water oxidation (Figure S4). Thus, the low absorbance of the $FeNiO_x$ film is due to its lower loading. SEM images of the FTO electrodes before and after the deposition of the NiO_x and $FeNiO_x$ catalysts are shown in Figure 3b. The NiO_x catalyst has a nanosheet morphology similar to other Ni-based OER catalysts.[37] On the other hand, high-resolution SEM images revealed no perceivable difference

DOI: 10.1021/jacs.5b05544
J. Am. Chem. Soc. 2015, 137, 9927−9936

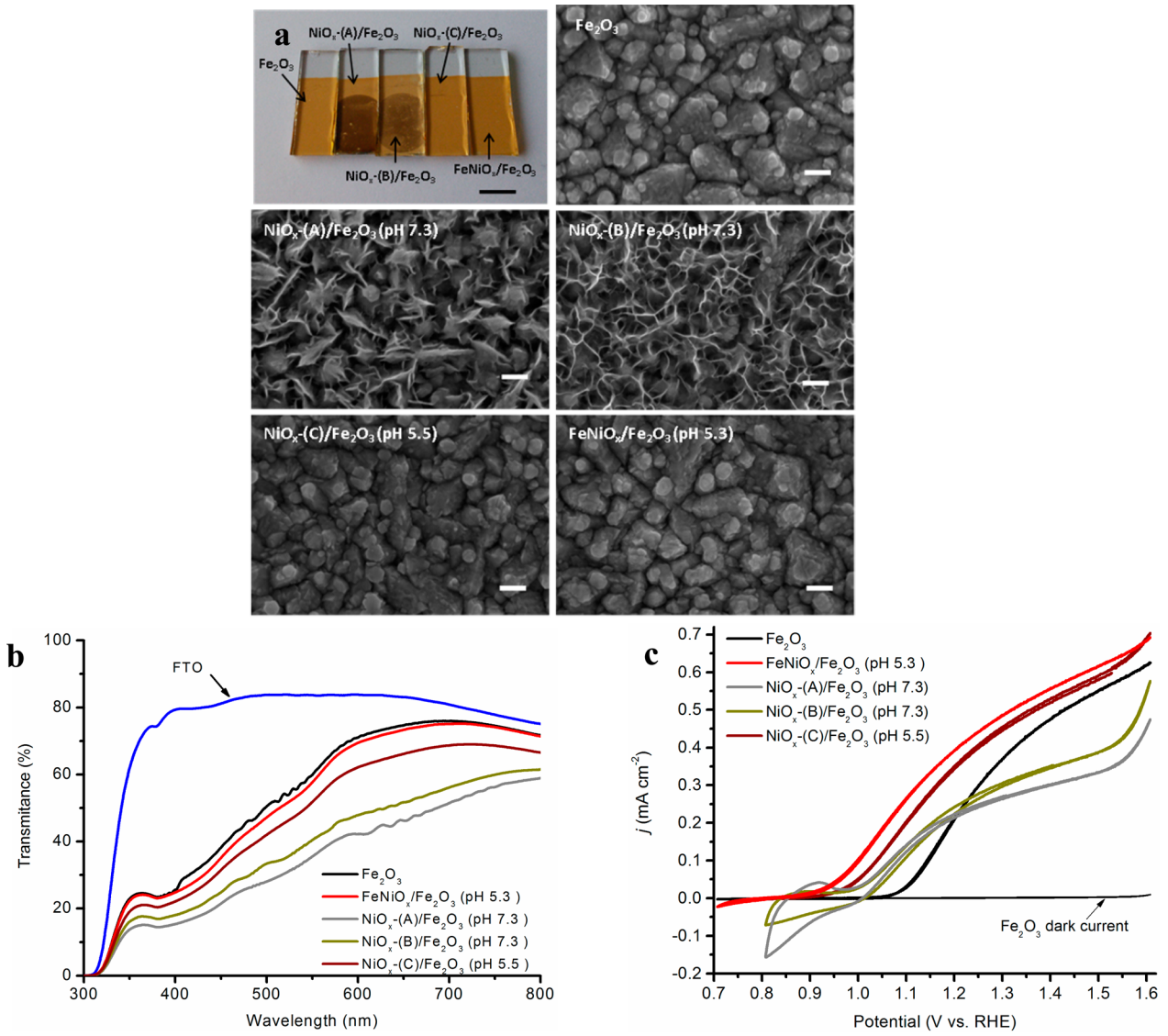

Figure 4. OER catalysts on hematite flat films for photoelectrochemical oxygen evolution. (a) Optical and SEM images of hematite films coated with different OER catalysts. The digital image in the top left was taken after a certain period of electrocatalysis in order to bring the catalyst into the active (oxidized) state. Each photoelectrode has dimensions of 12 × 30 mm and the size bar in the digital picture corresponds to 10 mm. An SEM image of Fe_2O_3 before any OER catalyst deposition is shown for comparison. Scale bars in the SEM images correspond to 200 nm. (b) Light transmittance of catalyst-coated hematite thin film OER photoelectrodes. The catalysts were deposited by 50 linear voltage sweeps. (c) Cyclic voltammograms of oxygen evolution under AM 1.5 illumination (1 sun) for hematite flat film photoanodes coated with NiO_x and $FeNiO_x$ catalysts. The scan rate is 1 mV s^{-1}, illumination is from the front (catalyst side) and the electrolyte is 1.0 M KOH (pH 13.6). The reduction and oxidation waves for the photoanodes at potentials between 0.8 and 1.0 V vs RHE correspond to the reduction and oxidation of the catalyst on the surface of the hematite before the onset of oxygen evolution. The $FeNiO_x/Fe_2O_3$ is optically transparent and shows the same performance when illuminated from the back side (FTO side) as shown in Figure S10. Dark currents are not shown here for simplicity but are found in the Supporting Information.

between the bare FTO electrode and the FTO electrode coated with a $FeNiO_x$ catalyst. This indicates that the $FeNiO_x$ film is very thin and conformal. Film thickness, estimated from the deposited catalyst mass (between 2 and 3 μg cm^{-2}) and the density of the known iron oxide and nickel hydroxide phases (5.3 g cm^{-3} for Fe_2O_3 and 4.1 g cm^{-3} for $Ni(OH)_2$), ranged from 4 to 7 nm. Cross-section SEM image of the $FeNiO_x$ film on FTO also indicates that the catalyst film is less than 10 nm in thickness (Figure S5). The exact structure or phase of the $FeNiO_x$ film is subject to further study, for example using X-ray absorption spectroscopy.[13,41] Segregation of phases or composition is possible.

The OER activity of NiO_x and $FeNiO_x$ catalysts were studied using linear sweep voltammetry (Figure 3c). For convenience of comparison, Au-coated quartz crystals were used as substrate because the loading of catalysts could be accurately determined by ECQM. The background OER activity of Au is low, and the activity of the catalyst is similar on Au and FTO (Figure 3c). For NiO_x, the activity increases as the number of linear sweeps increases; good activity was obtained after 150 consecutive linear sweeps. For $FeNiO_x$, the activity is similar for films made of 10, 30, and 150 sweep cycles (Figure S6b). The NiO_x and $FeNiO_x$ films, both made of 150 sweep cycles, were used for comparison. The NiO_x films have high activity, reaching 80 mA cm^{-2} at η < 400 mV overpotential (Figure 3c). The $FeNiO_x$ catalyst is comparatively less active. The current density is about 10 mA cm^{-2} at η < 400 mV.

DOI: 10.1021/jacs.5b05544
J. Am. Chem. Soc. 2015, 137, 9927−9936

For comparison of intrinsic activity of the catalyst, turnover frequency (TOF) should be used. In this case, the activity averaged over the total number of mols of the active metal ions is a good estimate of practical turnover frequency. Figure 3d and Figure S6a show that the $FeNiO_x$ catalyst is more active than the NiO_x catalyst at similar loadings. Assuming that all Ni ions are active in $FeNiO_x$, the turnover frequencies for OER are 1.1 and 9.1 s^{-1} at η = 0.35 and 0.4 V, respectively for a catalyst loading of 3.0 μg cm^{-2} (Figure 3d). For NiO_x at this loading, the turnover frequency is below 0.17 s^{-1} at η = 0.35 V (Figure S6a).

The turnover frequency of $FeNiO_x$ at η = 0.4 V (9.1 s^{-1}) is similar to the turnover frequency of IrO_x films (4.5−6 s^{-1}) at η = 0.68 V at pH 1.5 to 13.[42] Thus, the $FeNiO_x$ catalyst is much more active than IrO_x. At η = 0.35 V, the measured TOF of 1.1 s^{-1} for the $FeNiO_x$ electrocatalyst is comparable to that of other highly active thin film metal oxides OER catalysts recently reported (Figure 3d). For example, Trotochaud et al. found a TOF at η = 0.35 V of 2.8 s^{-1} for a $Ni_{0.9}Fe_{0.1}O_x$ electrocatalyst prepared by a solution synthesis method with a catalyst loading of 1.17 μg cm^{-2}.[14] It is noted that lower catalyst loadings generally result in higher calculated TOFs. This trend can be observed in Figure S6a where the TOF of some of the most active Earth-abundant OER catalysts has been plotted versus the loading of the catalyst. Because the absorption of light by the catalyst layer is approximately proportional to the catalyst loading, an ideal OER catalyst for solar water splitting should be closer to the upper left corner of the plot in Figure S6.

The high turnover frequency of $FeNiO_x$ catalyst implies that the deposition of a small amount of this catalyst, which will be visibly transparent, should facilitate OER catalysis on a hematite photoanode without absorbing light. This will allow a front illumination which in turn can be utilized in a stacked tandem water splitting cell. The advantage of the new electrodeposition method is that it could be easily translated into photoelectrochemical deposition, as shown below.

Photoelectrochemical Deposition of OER Catalysts on Hematite Thin Films. For convenience of study, flat thin films of hematite were first used for photoelectrochemical (PEC) deposition of OER catalysts. In thin hematite flat films, the majority of light absorption takes place close to the semiconductor/electrolyte interface where the photogenerated holes can be extracted efficiently from the hematite. Moreover, the measured photocurrents are essentially independent of the direction of illumination (front- vs backside), allowing the study of photoelectrochemical water oxidation even when one side of the hematite is covered by a light-absorbing OER catalyst. Three different conditions were used for the deposition of NiO_x. NiO_x-(A) was photoelectrodeposited from a Ni(II) acetate solution at pH 7.3 by linear sweep voltammetry between 1.0 and 1.6 V vs RHE under AM 1.5 illumination (100 mW cm^{-2}) from the back side of the photoanode. The photoelectrode turned dark after a few cycles as shown in Figure 4a. NiO_x-(B) was deposited using the same number of cycles (50 cycles) but in a narrower potential window between 1.0 and 1.2 V vs RHE. The NiO_x-(C) catalyst was deposited in the potential window between 1.0 and 1.2 V vs RHE but at pH 5.5.

XPS spectra of the NiO_x catalysts on hematite are similar to those of typical NiOOH-type catalysts (Figure S7). HR-SEM images of the hematite flat films before and after deposition of the NiO_x catalysts are shown in Figure 4a. The NiO_x-(A) and NiO_x-(B) catalysts are visible as nanosheets, and the sheets are smaller in size for NiO_x-(B), indicating an influence by the deposition potential window. A similar observation was earlier made in the electrodeposition of NiO_x from a solution of nickel acetate, where the oxygen evolution at higher potentials was found to hinder the nucleation rate of NiO_x.[36] The NiO_x-(C) catalyst has a lower loading, is thinner, and allows a higher transmittance of light than the same material deposited at higher pH (Figure 4b).

Cyclic voltammetry under illumination revealed a $Ni(OH)_2$/NiOOH couple at 0.79 V vs RHE at pH 13.6 (Figure S8). In the dark, the $Ni(OH)_2$/NiOOH couple on hematite was observed at 1.3 V vs RHE, which is the same as on FTO. The photovoltage generated by the hematite flat film can be estimated from the shift of the potential of the $Ni(OH)_2$/NiOOH couple under illumination. Thus, the photovoltage is about 0.5 V. This value is in agreement with the open-circuit potential measurements of NiO_x/Fe_2O_3 photoelectrodes (Figure S9).

The performance of the three NiO_x/Fe_2O_3 photoanodes in PEC oxygen evolution is compared in Figure 4c. The NiO_x-(C) catalyst absorbs only a small portion of light (Figure 4a and 4b). Thus, front illumination was carried out. An improvement in the onset potential (defined by Le Formal et al.[43] as the potential at which the derivative of the photocurrent−potential curve becomes greater than 0.2 mA cm^{-2} V^{-1}) by 130 mV and an increase in photocurrent compared to bare hematite film was observed. The NiO_x-(A) and NiO_x-(B) catalysts absorb significantly the light during front illumination (Figure 4a and 4b) and reduce the light intensity reaching the hematite, lowering the photocurrents at higher bias potential (Figure 4c). Illumination was then carried out from the back side. The NiO_x catalysts gave an average improvement of about 120 mV on the onset potential (Figure S10).

While onset potential is commonly used as a metric to characterize the PEC OER, this potential should be determined with caution due to the possible interference of noncatalytic oxidation of catalysts before real OER current begins. Figure S11a shows the difference in the observed onset potential for NiO_x/Fe_2O_3 at different scan rates. When scanned from 0.4 V at a scan rate of 10 mV s^{-1}, an apparent onset potential for water oxidation was observed at 0.6 V vs RHE. When scanned at 1 mV s^{-1} by cyclic voltammetry, the onset potential was observed at 0.85 V vs RHE. The oxidation current at 0.6 V observed at faster scan rate is in fact due to the oxidation of catalyst from Ni(II) to Ni(III). Scanning in both directions by cyclic voltammetry should reveal the redox behavior of a catalyst on the surface of the photoelectrode even when using faster scan rates (Figure S11a) and allow the differentiation of catalyst oxidation from PEC water oxidation at low applied bias. In the literature, PEC OER is commonly carried out with a scan rate of 10 mV s^{-1} or greater. Verification of reported onset potentials under those conditions is out of the scope of this study. For a more meaningful comparison of selected OER catalysts on hematite, we decided to determine their onset potentials using 1 mV s^{-1} by cyclic voltammetry (see below), and also to verify that the currents near the onset potential were stable with potentiostatic experiments.

The $FeNiO_x$ catalyst was deposited by linear sweep voltammetry between 1.0 and 1.2 V vs RHE under simulated AM 1.5 illumination (100 mW cm^{-2}). The deposition of catalyst is independent of front or back illumination. The loading after 50 linear sweeps was estimated to be 1.5−2 μg cm^{-2} from the increase in absorbance (decrease in trans-

DOI: 10.1021/jacs.5b05544
J. Am. Chem. Soc. 2015, 137, 9927−9936

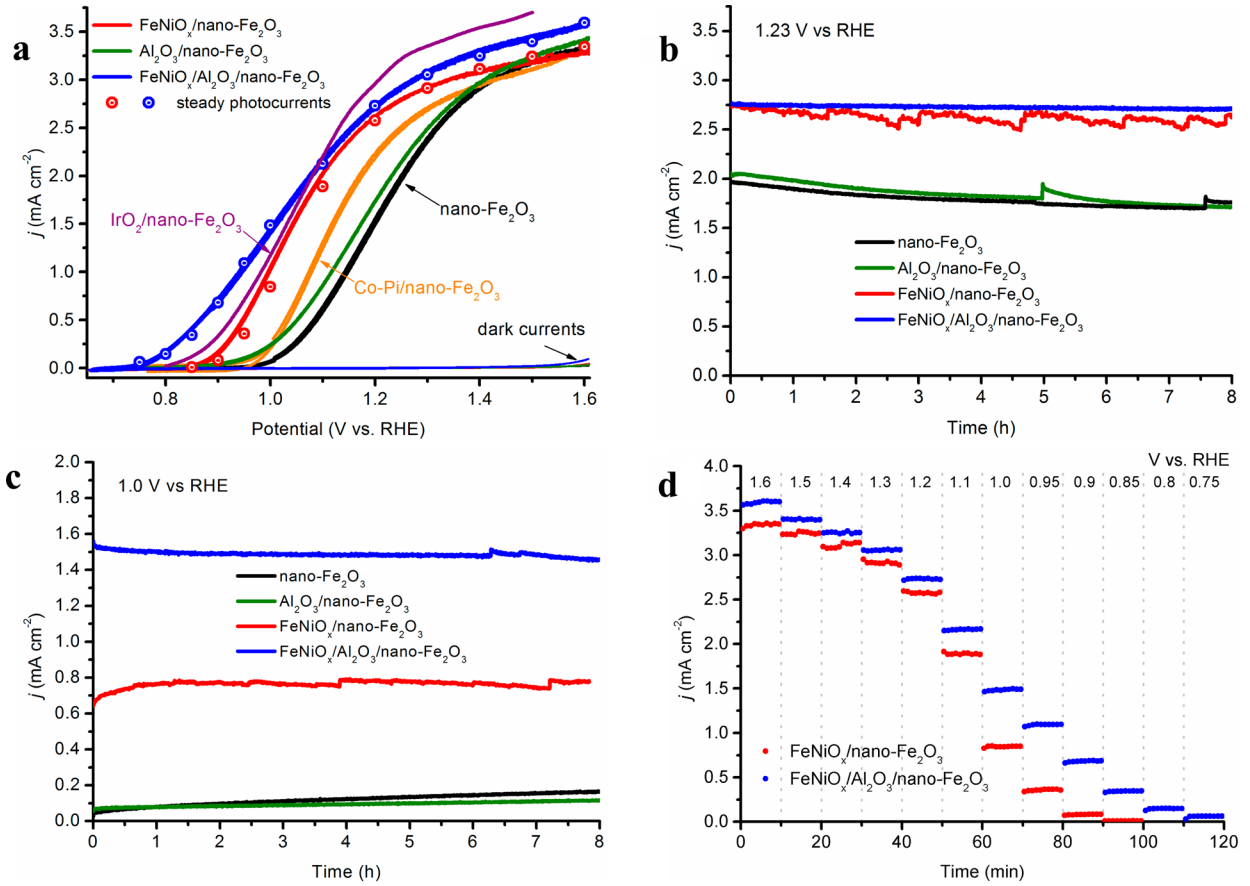

Figure 5. Photoelectrocatalytic activity and stability measurements on cauliflower-type hematite. (a) Cyclic voltammograms of OER under AM 1.5 illumination (1 sun) for nano-Fe_2O_3 photoanodes coated with different catalysts and ultrathin Al_2O_3. Scan rate is 1 mV s^{-1} and illumination is from the front (catalyst side). The data for IrO_2/nano-Fe_2O_3 are shown for comparison; the values are taken from ref 39. Steady currents correspond to the average values at each potential extracted from (d). (b) Stability of PEC OER at 1.23 V vs RHE and (c) at 1.0 V vs RHE under AM 1.5 illumination (1sun) at pH 13.6. (d) Steady-state photocurrents at different potentials.

mittance) after the deposition of the catalyst on Fe_2O_3. Like on FTO, the $FeNiO_x$ catalyst was nearly optically transparent on hematite, confirmed by the optical image and transmittance spectra (Figure 4a and 4b). SEM images revealed the conformal nature of the catalyst (Figure 4a) and XPS measurements confirmed the deposition of $FeNiO_x$, with a Fe:Ni ratio of approximately 70:30 (Figure S7). Upon front illumination, the $FeNiO_x$ catalyst gave an improvement of more than 200 mV for the onset potential of OER (Figure 4c).

Recently, Berlinguette and co-workers reported a novel method to deposit amorphous $NiFeO_x$ catalyst by photo-decomposition of a metal−organic precursor.[10] This catalyst was applied by the group of Wang for OER on hematite where a significant reduction of onset potential was observed.[20] The thickness of the $NiFeO_x$ catalyst is on the order of 100 nm by this method, so the catalyst absorbs a significant portion of light. Therefore, light transmittance is low and only back illumination for $NiFeO_x$-coated hematite is possible, which makes this catalyst unsuitable for a stacked tandem cell. Nevertheless, we decided to compare our $FeNiO_x$ catalyst under front illumination with the $NiFeO_x$ catalyst under back illumination, using the slow scanning method (see above). Although the two catalysts gave a similar improved photocurrent at 1.2 V vs RHE, the onset of PEC OER took place at lower overpotential with $FeNiO_x$ catalyst (Figure S11b). Furthermore, the onset of OER current on $NiFeO_x$-coated hematite is masked by the oxidation of the catalyst, as evidenced by the significant reduction current of the catalyst on the return, cathodic scan. In short, the newly developed $FeNiO_x$ catalyst also outperformed the best reported $NiFeO_x$ catalyst on hematite in terms of net catalytic performance at low applied bias potential.

The roles of redox active oxide species in PEC OER by hematite are subject to debate in the literature and are perhaps dependent on the nature of the oxide species and the deposition methods. While the elucidation of the role of $FeNiO_x$ catalyst is the subject of a follow up study, some preliminary data is presented here. The flat band potential of hematite thin films measured by Mott−Schottky analysis did not change after the deposition of $FeNiO_x$ and was between 0.5 and 0.6 V vs RHE under illumination (Figure S12). Likewise, the open-circuit photovoltages of bare hematite and hematite coated with NiO_x or $FeNiO_x$ are all between 0.5 and 0.6 V (Figure S9).The effect of $FeNiO_x$ was further probed using electrochemical impedance spectroscopy. An impedance model proposed by Klahr et al. was used to fit the impedance data (Figure S13a).[18] The total resistance determined from the fitting parameters ($R_{impedance} = R_s + R_{ct} + R_2$) agrees with the resistance measured as the derivative of the current potential curve, $R_{measured}$ (Figure S13b). Here, R_s is the solution resistance, R_{ct} is the resistance to charge transfer for water oxidation and R_2 is the back electron recombination resistance

DOI: 10.1021/jacs.5b05544
J. Am. Chem. Soc. 2015, 137, 9927−9936

associated with a process taking place at frequencies of 100−1000 Hz or time constants of 1−10 ms. The resistance to charge transfer is observed at around 1 Hz and corresponds to a time constant in the order of 1 s. The distinction of the two processes has been previously reported by Le Formal et al.[44] Upon deposition of $FeNiO_x$, the charge transfer resistance, R_{ct}, decreased by more than 2 orders of magnitude at 0.8 V vs RHE, indicating a more facile OER (see Figure S13c and S13d). Thus, the $FeNiO_x$ appears to improve the OER kinetics. The capacitance of the surface states, C_{ct}, decreases with the deposition of the $FeNiO_x$ catalyst. Klahr et al. showed that the capacitance of similar states on hematite flat films increased with the deposition of a Co-Pi catalyst, giving evidence of hole storage through the Co-Pi catalyst film.[18] This seems not to be the case for the ultrathin $FeNiO_x$ catalyst reported here. Moreover, capacitive current due to the accumulation and depletion of holes was not observed before the onset of PEC water oxidation between 0.7 and 0.85 V vs RHE in Figure 4c while it is observed for the NiO_x catalysts.

Photoelectrochemical Deposition of $FeNiO_x$ Catalyst on Nanostructured Cauliflower-Type Hematite. Having identified $FeNiO_x$ as an active and optically transparent OER catalyst on flat hematite, this catalyst was deposited on nanostructured hematite, nano-Fe_2O_3. Nanostructured photoanodes are less amenable to common catalyst deposition methods such as spin coating and sputtering due to their high porosity and the difference of wettability between catalyst precursors and the surface of the photoelectrodes. On the other hand, PEC deposition is a suitable method. Indeed, $FeNiO_x$ could be deposited on the cauliflower-type hematite using the method similar to the deposition of $FeNiO_x$ on thin film hematite (Figure S14a). It was previously shown that deposition of a thin layer of Al_2O_3 by ALD on nanostructured hematite led to passivation of surface trap states and lowered the onset potential for OER.[45] Therefore, prior to the deposition of the $FeNiO_x$ catalyst, a cauliflower hematite was coated with an ultrathin layer (<1 nm) of Al_2O_3. The Fe 2p, Ni 2p and O 1s XPS spectra of the $FeNiO_x/Al_2O_3$/nano-Fe_2O_3 electrode are similar to the spectra of the $FeNiO_x/Fe_2O_3$ electrode, with a Fe:Ni ratio of 60:40 (Figure S7). The SEM image of $FeNiO_x/Al_2O_3$/nano-Fe_2O_3 is visually indistinguishable from the image of pristine nano-Fe_2O_3 (Figure S15), indicating a conformal coating of the $FeNiO_x$ catalyst.

A $FeNiO_x/Al_2O_3$/nano-Fe_2O_3 composite film was peeled from the electrode and subjected to TEM measurements (Figure S16). The diffraction planes observed by electron diffraction correspond to those observed by XRD in Figure S15c. The nano-Fe_2O_3 consists of several particle mosaics, each with a single principal crystallographic orientation (Figure S16b-h). Warren et al.[46] suggested that nanoparticle hematite aggregates with a single crystallographic orientation and low-angle grain boundaries within the domains of a mosaic have lower potential barriers, creating a percolation network that facilitates electronic transport. This morphology was observed to be advantageous for PEC OER on hematite photoanodes. We found similar nanoparticle aggregates in the highly active nano-Fe_2O_3. Thus, deposition of $FeNiO_x$ and Al_2O_3 did not disrupt the morphology of nano-Fe_2O_3. Sonication of the $FeNiO_x/Al_2O_3$/nano-Fe_2O_3 nanostructures in methanol before TEM analysis caused the partial detachment of the catalyst film from the hematite grains (Figure S17). Films with lengths of up to 400 nm in length were observed. Selected area electron diffraction patterns indicate that the film contains small domains of crystallinity, too small to be detected by XRD. A more thorough characterization of these films was difficult due to the instability of the Fe−Ni oxyhydroxide thin films under prolonged exposure to the electron beam.

Figure S14b shows that the $FeNiO_x$ catalyst shifted the onset potential for OER on nano-Fe_2O_3 proportionally to the number of linear sweeps used for the photoelectrochemical deposition of the catalyst. The onset potential with a catalyst deposited by 30 linear sweeps is 0.8 V vs RHE (Figure 5a). In comparison, Co-Pi deposited on nano-Fe_2O_3 has been reported to improve the onset potential to 0.9 V vs RHE.[21] Thus, the thin $FeNiO_x$ catalyst gives a 100 mV improvement compared to the state-of-the art Co-Pi catalyst on nanostructured hematite and is equally active as the previously reported IrO_2 nanoparticles.[39] It is noted that under the slow scan conditions used in this work, the improvement in the onset potential for the Co-Pi/nano-Fe_2O_3 is less than previously reported[21] (Figure 5a). The dependence of the apparent onset of photocurrent on the scan rate for Co-Pi/nano-Fe_2O_3 photoanodes is shown in Figure S18a. The improvement in onset potentials is highly reproducible for many $FeNiO_x$/nano-Fe_2O_3 photoanodes tested, with illuminated surface areas between 0.2 and 1.0 cm^2. Inclusion of an ultrathin layer (<1 nm) of Al_2O_3 further shifted the onset potential to 0.7 V vs RHE. The Al_2O_3 layer alone had much less effect in promoting the photocurrent than the $FeNiO_x$ layer alone (Figure 5a). The $FeNiO_x/Al_2O_3$/nano-Fe_2O_3 electrode exhibited a photocurrent of 1.5 mA cm^{-2} at 1.0 V vs RHE, which surpasses the state-of-the-art cauliflower-type nano-Fe_2O_3 electrode coated with Al_2O_3 as promoter and IrO_2[39] or Co-Pi as catalyst (Figure S18b).[47] Moreover, the $FeNiO_x$ is much more robust than the IrO_2 catalyst. Figure S18c shows that IrO_2 nanoparticles detached from nano-Fe_2O_3 electrode and the photocurrent decayed to the base values of bare nano-Fe_2O_3 within a few minutes. On the contrary, photocurrents of $FeNiO_x$/nano-Fe_2O_3 and $FeNiO_x/Al_2O_3$/nano-Fe_2O_3 electrodes are stable for hours (Figure 5b and 5c).

To further differentiate OER from oxidation of the catalyst, the photoanode was first biased at very oxidative potentials and slowly stepped toward the OER onset potential. As shown in Figure 5d, the steady state photocurrents are in excellent agreement with the photocurrents recorded using slow-scan cyclic voltammetry, even at 0.75 V vs RHE. The photocurrents are stable at 1.23 and 1.0 V vs RHE for at least 8 h under continuous front illumination (Figure 5b and 5c). In addition, Faradaic efficiency for oxygen evolution measured at 1.0 V vs RHE is 100%, within experimental error (Figure S19). Integration of the incident photon to current efficiency (IPCE) over the AM 1.5 solar spectrum is in agreement with the photocurrents observed at 1.0 and 0.8 V vs RHE (Figure S20). The spectral response of hematite biased at 1.0 V vs RHE agrees with its known bandgap of 2.0 eV.

Nanostructured Hematite/Perovskite Tandem Cell. Finally, we investigated the coupling of hematite to a perovskite solar cell to demonstrate unbiased overall water splitting (Figure 6). The photogenerated holes, the minority carriers in the n-type hematite, are transferred to the transparent OER catalyst in order to evolve oxygen, while the excited electrons flow to the ohmic contact with the perovskite solar cell. Light absorption in the perovskite cell also generates electron/hole pairs. The holes are driven to the back contact to recombine with the electrons from the hematite photoanode. The excited electrons in the perovskite cell are transferred through a wire to a nickel−molybdenum hydrogen evolution catalyst to evolve

DOI: 10.1021/jacs.5b05544
J. Am. Chem. Soc. 2015, 137, 9927−9936

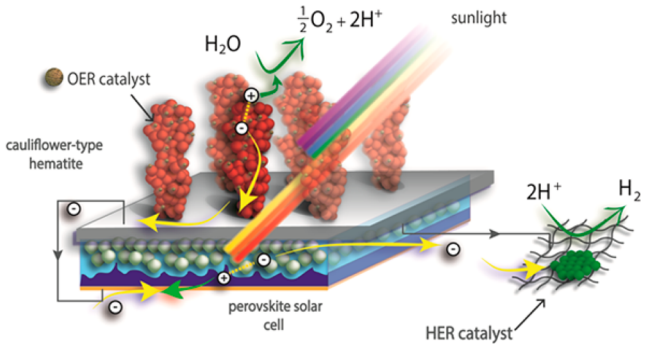

Figure 6. Unassisted water splitting using a nanostructured hematite/perovskite solar cell in a tandem configuration. Photons with energy higher than the band gap of hematite are absorbed in the top photoanode, while photons with lower energy are transmitted to the perovskite solar cell below.

hydrogen and complete the splitting of water. Recently, the groups of Mathews[48] and Kamat[49] reported similar photoanode/perovskite tandem cells systems for unassisted water splitting.

The procedure to couple the $FeNiO_x/Al_2O_3$/nano-Fe_2O_3 is similar to that of the coupling of Co-Pi/Al_2O_3/nano-Fe_2O_3 photoanode to a dye-sensitized solar cell (DSC) recently reported by one of our groups.[47] Figure S21 shows the digital images of the hematite and perovskite cell connected in series. Cauliflower-type hematite absorbs light below 620 nm while the $TiO_2/CH_3NH_3PbI_3$ perovskite cell has an incident-photon-to-current efficiency of over 80% between 750 and 400 nm[50] (Figure 7a). The maximum current density of the perovskite cell located in the back of the hematite photoanode can be predicted from the IPCE response of $TiO_2/CH_3NH_3PbI_3$ and the light transmittance of the hematite.[47] The predicted photocurrent is 11.0 mA cm^{-2} (Figure 7a). The maximum photocurrent for the $TiO_2/CH_3NH_3PbI_3$ measured in the tandem configuration immersed in solution is 12.2 mA cm^{-2} (Figure 7b). The observed difference (less than 10%) can be attributed to the spectral mismatch between the light source and the solar spectrum. The crossover point for the hematite photoanode and the perovskite solar cell is shown in Figure 7b and is close to 1.01 V vs RHE, with a current density of 1.6 mA cm^{-2}. This photocurrent corresponds to a STH efficiency of 2.0%. In comparison, the crossover photocurrent and STH efficiency for the reference Co-Pi/Al_2O_3/nano-Fe_2O_3 photoanode is 0.94 mA cm^{-2} and 1.2%, respectively (Figure 7b). Thus, the $FeNiO_x$ catalyst leads to significantly higher photocurrent than the Co-Pi catalyst for this system. The photocurrents measured in a three electrode configuration, where the hematite/perovskite tandem is the working

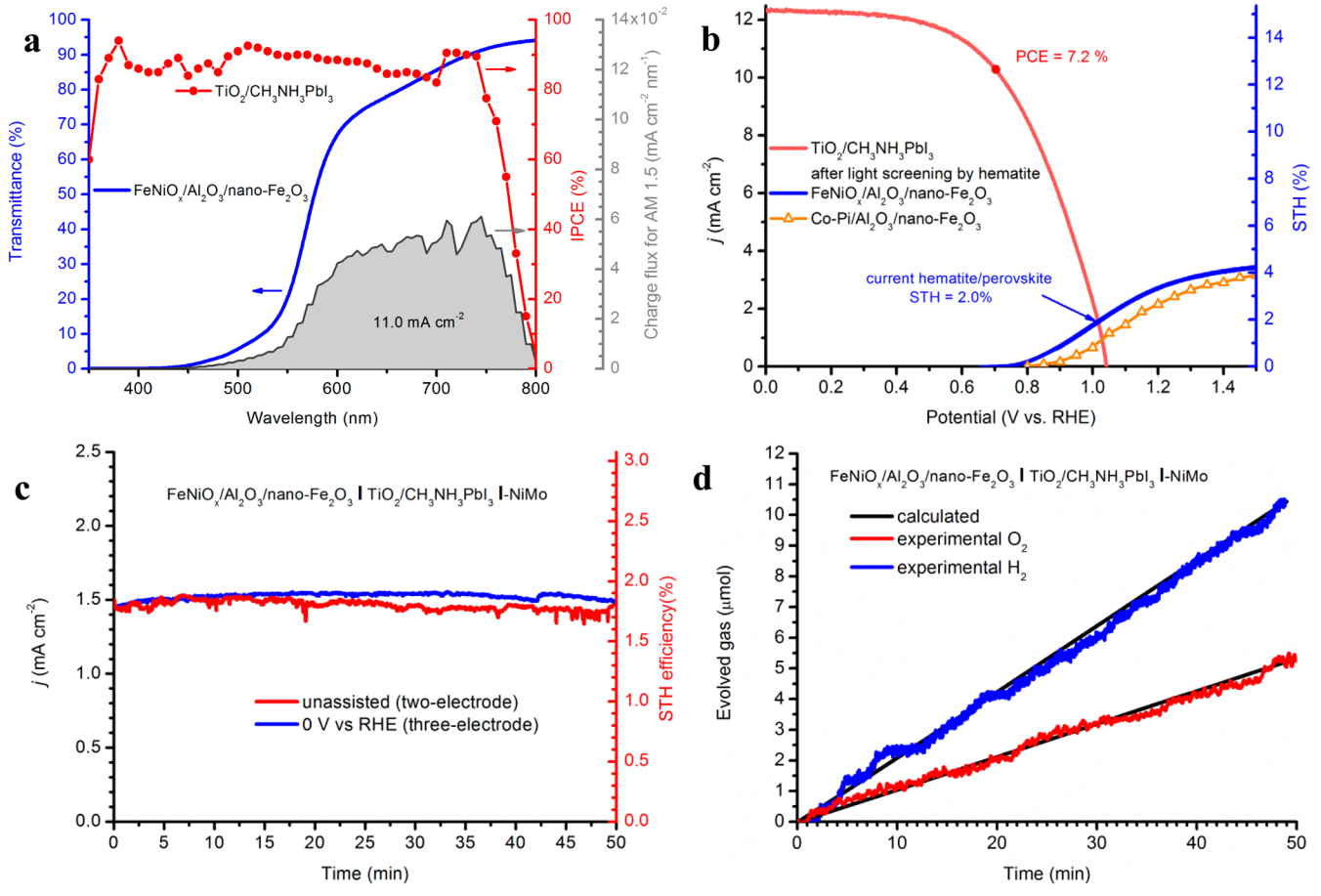

Figure 7. Hematite/perovskite tandem cell. (a) Transmittance of the hematite photoanode with the deposited Al_2O_3 and OER catalyst and IPCE of the $TiO_2/CH_3NH_3PbI_3$ perovskite photovoltaic. Charge flux calculated over the AM 1.5 solar spectrum is shown in the right axes. (b) Photocurrent crossover point for hematite and perovskite solar cell after light screening from the top hematite electrode. (c) Photoelectrochemical water splitting on hematite/perovskite tandem cell under simulated AM 1.5 illumination. (d) Quantification of H_2 and O_2 produced during photoelectrochemical water splitting.

DOI: 10.1021/jacs.5b05544
J. Am. Chem. Soc. 2015, 137, 9927−9936

electrode, are shown in Figure S22a. Ni−Mo, one of the best hydrogen evolution catalysts in alkaline solutions, was deposited on nickel foam to evolve hydrogen in the cathode with comparable catalytic activity to Pt in the region of low overpotential (Figure S23).[51] The geometric surface area of the Ni−Mo cathode was twice that of the hematite/perovskite tandem cell active area. During unassisted water splitting the Ni−Mo cathode was positioned 5 mm above the active area in front of the hematite photoanode so that it did not interfere with the illumination. Photocurrents at 0 V vs RHE are close to 1.54 mA cm^{-2} (1.9% STH efficiency), and similar values are observed in the two-electrode configuration during unassisted water splitting in the tandem cell due to the low overpotential required to drive the evolution of hydrogen on the Ni−Mo electrode (Figure 7c). This is one of the highest STH efficiencies for a hematite-based tandem water splitting device. In comparison, the Co-Pi/Al_2O_3/nano-Fe_2O_3/DSC tandem cell has an effective STH efficiency of 1.17%.[47] The average Faradaic efficiency for the tandem device during 45 min, after an initial period of 5 min to allow the stabilization of the system, is 101% ± 6% for H_2 and 100% ± 8% for O_2, indicating that the extracted charges are efficiently transformed into H_2 and O_2 (Figure 7d). The hematite/perovskite tandem cell shows good stability during prolonged water splitting measurements. The tandem cell retains 70% of the initial photocurrent after 8 h of testing (Figure S22b). Failure of all the tandem cells tested was observed only due to filtering of the solution through the encapsulating layer with time, which results in the quick dissolution of the perovskite cell.

Despite light screening by hematite below 620 nm, the perovskite cell has a maximum power conversion efficiency (PCE) of close to 7.2%, with a corresponding current density >10 mA cm^{-2}. Optimization of nanostructured hematite to match these currents is critical for the improvement of STH efficiency to a practical value. Nevertheless, the work demonstrates the utility of the transparent $FeNiO_x$ catalyst in this type of tandem cells. Other dual-absorber tandem cells have been recently reported. Van de Krol and co-workers showed that a tungsten-doped bismuth vanadate photoanode coupled to a single-junction amorphous silicon solar cell could split water with ∼3.7% STH efficiency under 1 sun illumination at pH ∼ 7.3 using a Co-Pi OER catalyst.[52] Brillet et al. reported unassisted water splitting with STH efficiencies of 3.1% at pH 0 for a WO_3/DSC system without using an OER catalyst.[47] Mathews and co-workers reported a Mn-doped hematite in tandem with a perovskite cell with Co-Pi as OER catalyst.[48] Although the initial current was 1.93 mA cm^{-2}, the photocurrent dropped to less than 1.7 mA cm^{-2} after 120 s. Co-Pi was also used as OER catalyst on a $BiVO_4$/perovskite tandem system with 2.5% STH efficiency operating at neutral pH.[49] The STH efficiency in this system also dropped to less than 2% after 300 s. The transparent $FeNiO_x$ catalyst developed here exhibit higher catalytic efficiency than Co-Pi (Figures 5a, 7b, S18b), and led to tandem cells with significantly better stability than analogous cells employing the Co-Pi catalyst.[48,49] Thus, it will be interesting to use this $FeNiO_x$ catalyst for other dual-absorber tandem cells.

CONCLUSIONS

In summary, we have developed oxidatively electrodeposited amorphous iron nickel oxide ($FeNiO_x$) as a novel oxygen evolution catalyst. The high turnover frequencies of the catalyst at modest overpotentials make it possible to efficiently evolve oxygen with loadings of a mere several μg cm^{-2}, which leads to optical transparency of the catalyst layer. The catalyst can be conveniently deposited onto photoanodes such as hematite by a simple photoelectrochemical method. Excellent photoelectrochemical performance for oxygen evolution is achieved with $FeNiO_x$-coated nanostructured hematite photoanodes. The optical transparency of the $FeNiO_x$ catalyst enables the preparation of a hematite/perovskite tandem water splitting cell. In a demonstration of principle, unassisted water splitting with solar-to-hydrogen conversion efficiencies in excess of 1.9% and ∼100% Faradaic efficiency was achieved. The development of the optically transparent and highly active $FeNiO_x$ catalyst and its successful integration into photoanodes open new opportunities in low-cost solar fuel production.

ASSOCIATED CONTENT

Supporting Information

The Supporting Information is available free of charge on the ACS Publications website at DOI: 10.1021/jacs.5b05544.

Detailed experimental procedures, characterization of the catalyst deposited on FTO and hematite photoanodes, and additional electrochemical and photoelectrochemical measurements. (PDF)

AUTHOR INFORMATION

Corresponding Author

*xile.hu@epfl.ch

Present Addresses

§(A.Y.) Department of Metallurgical Engineering and Materials Science, Indian Institute of Technology-Bombay, Powai, Mumbai-400076, India.

#(S.D.T.) Molecular Approaches to Renewable Energies, Department of Chemistry, University of Zurich, 8057 Zurich, Switzerland.

Notes

The authors declare no competing financial interest.

ACKNOWLEDGMENTS

The work at EPFL-LSCI is supported by a starting grant from the European Research Council (ERC), number 257096. The work at EPFL-LPI is supported by the Swiss Federal Office for Energy (PECHouse Competence Center, contract number SI/500090−02), the PECDEMO project (cofunded by Europe's Fuel Cell and Hydrogen Joint Undertaking under Grant Agreement No. 621252), the PHOCS project (European Union, ENERGY 2012-10.2.1, Future Emerging Technologies Collaborative Project no. 309223) and the European Research Council under the Advanced Research Grant (ARG 247404) "Mesolight". We thank Dr. Song Fang for help with the acquisition of TEM images.

REFERENCES

(1) Gratzel, M. *Nature* **2001**, *414*, 338−344.

(2) Tachibana, Y.; Vayssieres, L.; Durrant, J. R. *Nat. Photonics* **2012**, *6*, 511−518.

(3) Hu, S.; Xiang, C.; Haussener, S.; Berger, A. D.; Lewis, N. S. *Energy Environ. Sci.* **2013**, *6*, 2984−2993.

(4) Prévot, M. S.; Sivula, K. *J. Phys. Chem. C* **2013**, *117*, 17879−17893.

(5) Ronge, J.; Bosserez, T.; Martel, D.; Nervi, C.; Boarino, L.; Taulelle, F.; Decher, G.; Bordiga, S.; Martens, J. A. *Chem. Soc. Rev.* **2014**, *43*, 7963.

DOI: 10.1021/jacs.5b05544
J. Am. Chem. Soc. 2015, 137, 9927−9936

(6) Reece, S. Y.; Hamel, J. A.; Sung, K.; Jarvi, T. D.; Esswein, A. J.; Pijpers, J. J. H.; Nocera, D. G. *Science* **2011**, *334*, 645−648.
(7) Khaselev, O.; Turner, J. A. *Science* **1998**, *280*, 425−427.
(8) Licht, S.; Wang, B.; Mukerji, S.; Soga, T.; Umeno, M.; Tributsch, H. *J. Phys. Chem. B* **2000**, *104*, 8920−8924.
(9) Gong, M.; Li, Y.; Wang, H.; Liang, Y.; Wu, J. Z.; Zhou, J.; Wang, J.; Regier, T.; Wei, F.; Dai, H. *J. Am. Chem. Soc.* **2013**, *135*, 8452−8455.
(10) Smith, R. D. L.; Prévot, M. S.; Fagan, R. D.; Zhang, Z.; Sedach, P. A.; Siu, M. K. J.; Trudel, S.; Berlinguette, C. P. *Science* **2013**, *340*, 60−63.
(11) Smith, R. D. L.; Prévot, M. S.; Fagan, R. D.; Trudel, S.; Berlinguette, C. P. *J. Am. Chem. Soc.* **2013**, *135*, 11580−11586.
(12) Kanan, M. W.; Nocera, D. G. *Science* **2008**, *321*, 1072−1075.
(13) Louie, M. W.; Bell, A. T. *J. Am. Chem. Soc.* **2013**, *135*, 12329−12337.
(14) Trotochaud, L.; Ranney, J. K.; Williams, K. N.; Boettcher, S. W. *J. Am. Chem. Soc.* **2012**, *134*, 17253−17261.
(15) Yeo, B. S.; Bell, A. T. *J. Am. Chem. Soc.* **2011**, *133*, 5587−5593.
(16) Seabold, J. A.; Choi, K.-S. *Chem. Mater.* **2011**, *23*, 1105−1112.
(17) Li, J.; Meng, F.; Suri, S.; Ding, W.; Huang, F.; Wu, N. *Chem. Commun.* **2012**, *48*, 8213−8215.
(18) Klahr, B.; Gimenez, S.; Fabregat-Santiago, F.; Bisquert, J.; Hamann, T. W. *J. Am. Chem. Soc.* **2012**, *134*, 16693−16700.
(19) Kim, T. W.; Choi, K.-S. *Science* **2014**, *343*, 990−994.
(20) Du, C.; Yang, X.; Mayer, M. T.; Hoyt, H.; Xie, J.; McMahon, G.; Bischoping, G.; Wang, D. *Angew. Chem., Int. Ed.* **2013**, *52*, 12692−12695.
(21) Zhong, D. K.; Cornuz, M.; Sivula, K.; Gratzel, M.; Gamelin, D. R. *Energy Environ. Sci.* **2011**, *4*, 1759−1764.
(22) Seabold, J. A.; Choi, K.-S. *J. Am. Chem. Soc.* **2012**, *134*, 2186−2192.
(23) Shi, X.; Choi, Y.; Zhang, K.; Kwon, J.; Kim, D. Y.; Lee, J. K.; Oh, S. H.; Kim, J. K.; Park, J. H. *Nat. Commun.* **2014**, *5*, 4775.
(24) Corrigan, D. A.; Bendert, R. M. *J. Electrochem. Soc.* **1989**, *136*, 723−728.
(25) Trotochaud, L.; Mills, T. J.; Boettcher, S. W. *J. Phys. Chem. Lett.* **2013**, *4*, 931−935.
(26) Seger, B.; Castelli, I. E.; Vesborg, P. C. K.; Jacobsen, K. W.; Hansen, O.; Chorkendorff, I. *Energy Environ. Sci.* **2014**, *7*, 2397−2413.
(27) Riha, S. C.; Klahr, B. M.; Tyo, E. C.; Seifert, S.; Vajda, S.; Pellin, M. J.; Hamann, T. W.; Martinson, A. B. F. *ACS Nano* **2013**, *7*, 2396−2405.
(28) McKone, J. R.; Lewis, N. S.; Gray, H. B. *Chem. Mater.* **2014**, *26*, 407−414.
(29) Chen, Z.; Rathmell, A. R.; Ye, S.; Wilson, A. R.; Wiley, B. J. *Angew. Chem., Int. Ed.* **2013**, *52*, 13708−13711.
(30) Trotochaud, L.; Young, S. L.; Ranney, J. K.; Boettcher, S. W. *J. Am. Chem. Soc.* **2014**, *136*, 6744−6753.
(31) McCrory, C. C. L.; Jung, S.; Peters, J. C.; Jaramillo, T. F. *J. Am. Chem. Soc.* **2013**, *135*, 16977−16987.
(32) Merrill, M. D.; Dougherty, R. C. *J. Phys. Chem. C* **2008**, *112*, 3655−3666.
(33) Wehrens-Dijksma, M.; Notten, P. H. L. *Electrochim. Acta* **2006**, *51*, 3609−3621.
(34) Ding, Y.; Yuan, J.; Chang, Z. *J. Power Sources* **1997**, *69*, 47−54.
(35) Bendert, R. M.; Corrigan, D. A. *J. Electrochem. Soc.* **1989**, *136*, 1369−1374.
(36) Briggs, G. W. D.; Fleischmann, M. *Trans. Faraday Soc.* **1966**, *62*, 3217−3228.
(37) Wu, M.-S.; Yang, C.-H.; Wang, M.-J. *Electrochim. Acta* **2008**, *54*, 155−161.
(38) Schultze, J. W.; Lohrengel, M. M.; Ross, D. *Electrochim. Acta* **1983**, *28*, 973−984.
(39) Tilley, S. D.; Cornuz, M.; Sivula, K.; Grätzel, M. *Angew. Chem., Int. Ed.* **2010**, *49*, 6405−6408.
(40) Anodic deposition of an FeO_x film does not take place under the same conditions as the $FeNiO_x$ catalyst when only $Fe_2(SO_4)_3$ is used as precursor.
(41) Friebel, D.; Louie, M. W.; Bajdich, M.; Sanwald, K. E.; Cai, Y.; Wise, A. M.; Cheng, M.-J.; Sokaras, D.; Weng, T.-C.; Alonso-Mori, R.; Davis, R. C.; Bargar, J. R.; Nørskov, J. K.; Nilsson, A.; Bell, A. T. *J. Am. Chem. Soc.* **2015**, *137*, 1305−1313.
(42) Nakagawa, T.; Beasley, C. A.; Murray, R. W. *J. Phys. Chem. C* **2009**, *113*, 12958−12961.
(43) Le Formal, F.; Grätzel, M.; Sivula, K. *Adv. Funct. Mater.* **2010**, *20*, 1099−1107.
(44) Le Formal, F.; Pendlebury, S. R.; Cornuz, M.; Tilley, S. D.; Grätzel, M.; Durrant, J. R. *J. Am. Chem. Soc.* **2014**, *136*, 2564−2574.
(45) Le Formal, F.; Tetreault, N.; Cornuz, M.; Moehl, T.; Gratzel, M.; Sivula, K. *Chem. Sci.* **2011**, *2*, 737−743.
(46) Warren, S. C.; Voitchovsky, K.; Dotan, H.; Leroy, C. M.; Cornuz, M.; Stellacci, F.; Hebert, C.; Rothschild, A.; Gratzel, M. *Nat. Mater.* **2013**, *12*, 842−849.
(47) Brillet, J.; Yum, J. H.; Cornuz, M.; Hisatomi, T.; Solarska, R.; Augustynski, J.; Graetzel, M.; Sivula, K. *Nat. Photonics* **2012**, *6*, 823−827.
(48) Gurudayal; Sabba, D.; Kumar, M. H.; Wong, L. H.; Barber, J.; Graetzel, M.; Mathews, N. *Nano Lett.* **2015**, *15*, 3833−3839.
(49) Chen, Y.-S.; Manser, J. S.; Kamat, P. V. *J. Am. Chem. Soc.* **2015**, *137*, 974−981.
(50) Yella, A.; Heiniger, L.-P.; Gao, P.; Nazeeruddin, M. K.; Grätzel, M. *Nano Lett.* **2014**, *14*, 2591−2596.
(51) McKone, J. R.; Marinescu, S. C.; Brunschwig, B. S.; Winkler, J. R.; Gray, H. B. *Chem. Sci.* **2014**, *5*, 865−878.
(52) Abdi, F. F.; Han, L. H.; Smets, A. H. M.; Zeman, M.; Dam, B.; van de Krol, R. *Nat. Commun.* **2013**, *4*, 2195.

DOI: 10.1021/jacs.5b05544
J. Am. Chem. Soc. 2015, 137, 9927−9936